Noname manuscript No.
(will be inserted by the editor)

A Non-oscillatory Multi-Moment Finite Volume Scheme with Boundary Gradient Switching

Xi Deng · Ziyao Sun · Bin Xie · Kensuke Yokoi · Chungang Chen · Feng Xiao

Received: date / Accepted: date

Abstract In this work we propose a new formulation for high-order multi-moment constrained finite volume (MCV) method. In the one-dimensional building-block scheme, three local degrees of freedom (DOFs) are equidistantly defined within a grid cell. Two candidate polynomials for spatial reconstruction of third-order are built by adopting one additional constraint condition from the adjacent cells, i.e. the DOF at middle point of left or right neighbour. A boundary gradient switching (BGS) algorithm based on the variation-minimization principle is devised to determine the spatial reconstruction from the two candidates, so as to remove the spurious oscillations around the discontinuities. The resulted non-oscillatory MCV3-BGS scheme is of fourth-order accuracy and completely free of case-dependent ad hoc parameters. The widely used benchmark tests of one- and two-dimensional scalar and Euler hyperbolic conservation laws are solved to verify the performance of the proposed scheme in this paper. The MCV3-BGS scheme is very promising for the practical applications due to its accuracy, non-oscillatory feature and algorithmic simplicity.

Keywords Multi-moment method · Finite volume method · Variation-minimization principle · Non-oscillatory scheme · High-order scheme · Local reconstruction

This work was supported in part by JSPS KAKENHI (Grant No. 15H03916) and National Natural Science Foundation of China (Grant No. 41522504).

Xi Deng · Ziyao Sun · Bin Xie · Feng Xiao
Department of Mechanical Engineering, Tokyo Institute of Technology, 4259 Nagatsuta,Midori-ku, Yokohama, 226-8502, Japan.
E-mail: xiao@ex.titech.ac.jp (Feng Xiao)

Kensuke Yokoi
School of Engineering, Cardiff University, The Parade, Cardiff, CF24 3AA, UK.

Chungang Chen
School of Human Settlement and Civil Engineering, Xi'an Jiaotong University, Xi'an, Shaanxi 710049, China.
E-mail: cgchen@xjtu.edu.cn (Chungang Chen)

1 Introduction

As one of high-order schemes with local reconstructions, multi-moment constrained finite volume (MCV) method [10] has been applied in both incompressible [26,27] and compressible flows[10]. The MCV scheme is appealing to the practical applications due to its flexibility to grid structures and the proper balance between the accuracy and the complexity of numerical schemes. Same as other local high-order schemes such as discontinuous Galerkin (DG) method [3,2,7], the spectral volume (SV) method [23], the spectral difference (SD) method [20] and the constrained interpolation profile (CIP) [28,29,25] method, MCV schemes employ more than one local degrees of freedom (DOFs) within a local cell for a high-order spatial reconstruction. In MCV method, the point-wise values defined at solution points are adopted as DOFs and it's spatial diecretization formulations are derived by introducing the constraint conditions in terms of multi moments, including the point value (PV), the volume-integrated average (VIA) and the derivatives of the different orders of the physical fields.

According to well-known Godunov barrier for linear schemes, any monotonic linear scheme can be of only first order. As a result, the high-order MCV schemes will produce the non-physical oscillations while simulating the compressible flows, even for those cases with the smooth initial conditions where discontinuity will appear due to the nonlinearity of the governing equations. Several strategies have been employed by the local high-order schemes to suppress the numerical oscillations in the vicinity of discontinuities in the existing literature. One of the popular strategies is nonlinear limiting projection. Earlier studies such as in [3,2] for DG method and in [10] for MCV method use the total variation bounded (TVB) limiters, where the TVB criterion is needed to find the "troubled cells" by evaluating the smoothness of the solution. For the troubled cells, where discontinuous solutions are detected, the total variation diminishing (TVD) limiting procedure is applied. As the TVD limiting has second-order accuracy at most, it tends to introduce too much extra numerical dissipation and degrades the high-order accuracy of the original schemes. The higher order limited reconstructions, such as the essentially non-oscillatory (ENO) [6,17,16] and weighted essentially non-oscillatory (WENO) [11] reconstructions, are applied in [14,15,30] for DG method and in [21] for MCV method. The WENO limiter effectively reduces the numerical dissipation errors around smooth region and can retain the high-order convergence. However, the current implementations of the WENO limiting in the high-order schemes with local reconstructions cannot make the full use of the local DOFs, and the solutions are heavily dependent on the TVB criterion that determines the "troubled cells" in an ad hoc fashion. This is one of the key issues to be solved for developing numerical models for practical applications using local high-order schemes.

In this study, a new formulation for non-oscillatory three-point MCV scheme of fourth-order accuracy is proposed. Different from Hermite interpolation polynomial used in [21], where the first-order derivative at the cell center was employed to adjust numerical properties of the scheme, two cubic Lagrangian interpolation polynomials, which are constructed by using the DOFs in adjacent cells, are employed as candidates for spatial reconstruction. These two candidates are chosen through a new proposed boundary gradient switching (BGS) algorithm based on the underlying idea of the ENO method [6,17,16] to remove the non-physical oscillations near the discontinuity. Since two candidate polynomials give the fourth-

order accuracy, the proposed scheme is also expected to have the same convergence rate as verified by the numerical tests in this paper. The proposed scheme is implemented without any user-specifying ad hoc parameters. Furthermore, the stencil required by this new scheme still remains compact (within three cells), same as our previous study in [21].

The rest part of this paper is organized as follows. In section 2, the new formulation for non-oscillatory MCV scheme, called MCV3-BGS scheme, is described in detail. The widely used benchmark tests for scalar and Euler hyperbolic conservation equations in one- and two-dimensions are computed to verify the accuracy and the ability to resolve the discontinuous solutions of the proposed scheme in section 3. Finally, a brief conclusion is given in section 4.

2 Numerical formulations

We consider the following hyperbolic system in one dimension,

$$\frac{\partial \boldsymbol{q}}{\partial t} + \frac{\partial \boldsymbol{f}(\boldsymbol{q})}{\partial x} = 0, \tag{1}$$

where $\boldsymbol{q}$ is the vector of the dependent variables, and $\boldsymbol{f}(\boldsymbol{q})$ is the vector of the flux functions.

The computational domain is divided into I non-overlapping cells, e.g. $\mathcal{C}_i = [x_{i-\frac{1}{2}}, x_{i+\frac{1}{2}}]$ $(i = 1, 2, \cdots, I)$. Within the computational cell $\mathcal{C}_i$, the local DOFs are defined as the point-wise values q_{ik} $(k = 1, 2, \cdots, K)$ at solution points x_{ik}, which are updated using the governing equations of differential-form as

$$\frac{\partial \boldsymbol{q}_{ik}}{\partial t} = -\left(\frac{\partial \boldsymbol{f}(\boldsymbol{q})}{\partial x}\right)_{ik}. \tag{2}$$

Using the framework of MCV method [10], the constraint conditions in terms of different kinds of moments are adopted to derive the discretization formulation of the right-hand side term in (2).

2.1 Three-point MCV scheme

Here we briefly describe the numerical formulation for three-point MCV (MCV3) scheme, which is the basic framework for this study.

Within cell $\mathcal{C}_i$, three local DOFs are defined as the pointwise values as $\mathbf{q}_{i1}$, $\mathbf{q}_{i2}$ and $\mathbf{q}_{i3}$ at equidistantly arranged solution points $x_{i1} = x_{i-\frac{1}{2}}$, $x_{i2} = x_i$ and $x_{i3} = x_{i+\frac{1}{2}}$, where $x_i = (x_{i-\frac{1}{2}} + x_{i+\frac{1}{2}})/2$ is the center of cell $\mathcal{C}_i$.

Two kinds of moments are adopted to provide the constraint conditions for spatial discretization of the DOFs.

– **Point Values (PV)**
At the cell interface, e.g., $x = x_{i-\frac{1}{2}}$ PV moment is specified as

$$\overline{{}^{P}\boldsymbol{q}}_{i-\frac{1}{2}}(t) = \boldsymbol{q}\left(x_{i-\frac{1}{2}}, t\right). \tag{3}$$

– **Volume-Integrated Average (VIA)**
Over the cell $\mathcal{C}_i$, VIA moment is specified as

$$\overline{{}^{V}\boldsymbol{q}}_i(t) = \frac{1}{\Delta x}\int_{x_{i-\frac{1}{2}}}^{x_{i+\frac{1}{2}}} \boldsymbol{q}(x,t)\,dx. \tag{4}$$

The multi-moment constraint conditions are related with the local DOFs as

$$\begin{cases} \overline{{}^{P}\boldsymbol{q}}_{i-\frac{1}{2}} = \boldsymbol{Q}_i\left(x_{i-\frac{1}{2}}\right) = \boldsymbol{q}_{i1}, \\ \overline{{}^{P}\boldsymbol{q}}_{i+\frac{1}{2}} = \boldsymbol{Q}_i\left(x_{i-\frac{1}{2}}\right) = \boldsymbol{q}_{i3}, \\ \overline{{}^{V}\boldsymbol{q}}_i = \displaystyle\int_{x_{i-\frac{1}{2}}}^{x_{i+\frac{1}{2}}} \boldsymbol{Q}_i(x)\,dx = \frac{1}{6}\left(\boldsymbol{q}_{i1}+4\boldsymbol{q}_{i2}+\boldsymbol{q}_{i3}\right), \end{cases} \tag{5}$$

where $\boldsymbol{Q}_i(x)$ is a Lagrangian interpolation polynomial for physical field $\boldsymbol{q}(x)$ within cell $\mathcal{C}_i$, having the form of

$$\boldsymbol{Q}_i(x) = \sum_{k=1}^{3} \boldsymbol{q}_{ik}\phi_{ik}(x), \tag{6}$$

with Lagrangian basis function $\phi_{ik}(x)$ written as

$$\phi_{ik}(x) = \prod_{l=1,l\neq k}^{3} \frac{x-x_{il}}{x_{ik}-x_{il}}. \tag{7}$$

The different moments are updated by different formulations in our multi-moment schemes.

– PV moment is updated by differential-form governing equations as

$$\frac{\partial \overline{{}^{P}\boldsymbol{q}}_{i-\frac{1}{2}}}{\partial t} \approx -\hat{\boldsymbol{f}}_{xi-\frac{1}{2}}. \tag{8}$$

The derivative of flux function in (8) is evaluated by solving a derivative Riemann problem as

$$\hat{\boldsymbol{f}}_{xi-\frac{1}{2}} = \mathrm{dRiemann}\left(\hat{\boldsymbol{f}}^{-}_{xi-\frac{1}{2}}, \hat{\boldsymbol{f}}^{+}_{xi-\frac{1}{2}}\right), \tag{9}$$

where

$$\begin{cases} \hat{\boldsymbol{f}}^{-}_{xi-\frac{1}{2}} = \boldsymbol{A}_{i-\frac{1}{2}}\left(\frac{\partial \boldsymbol{Q}_{i-1}(x)}{\partial x}\right)_{i-\frac{1}{2}}, \\ \hat{\boldsymbol{f}}^{+}_{xi-\frac{1}{2}} = \boldsymbol{A}_{i-\frac{1}{2}}\left(\frac{\partial \boldsymbol{Q}_{i}(x)}{\partial x}\right)_{i-\frac{1}{2}}, \end{cases} \tag{10}$$

with $\boldsymbol{A}_{i-\frac{1}{2}}$ being the Jacobian matrix at cell interface $x = x_{i-\frac{1}{2}}$.

– VIA moment is updated by a flux-form formulation assuring the conservation of the proposed scheme as

$$\frac{\partial \overline{{}^{V}\boldsymbol{q}}_i}{\partial t} \approx -\frac{1}{\Delta x_i}\left(\hat{\boldsymbol{f}}_{i+\frac{1}{2}} - \hat{\boldsymbol{f}}_{i-\frac{1}{2}}\right), \tag{11}$$

where $\Delta x_i = x_{i+\frac{1}{2}} - x_{i-\frac{1}{2}}$ and the numerical flux at cell interfaces are computed directly from the DOFs readily available there as the computational variables, i.e. $\hat{\boldsymbol{f}}_{i-\frac{1}{2}} = \boldsymbol{f}(\boldsymbol{q}_{i1})$ and $\hat{\boldsymbol{f}}_{i+\frac{1}{2}} = \boldsymbol{f}(\boldsymbol{q}_{i3})$.

Using the constraint relation (5), the spatial discretization of DOFs within cell $\mathcal{C}_i$ are then determined from (8) and (11) as

$$\begin{cases} \frac{\partial \boldsymbol{q}_{i1}}{\partial t} = -\hat{\boldsymbol{f}}_{xi-\frac{1}{2}}, \\ \frac{\partial \boldsymbol{q}_{i2}}{\partial t} = -\frac{3}{2\Delta x_i}\left(\hat{\boldsymbol{f}}_{i+\frac{1}{2}} - \hat{\boldsymbol{f}}_{i-\frac{1}{2}}\right) + \frac{1}{4}\left(\hat{\boldsymbol{f}}_{xi-\frac{1}{2}} + \hat{\boldsymbol{f}}_{xi+\frac{1}{2}}\right), \\ \frac{\partial \boldsymbol{q}_{i3}}{\partial t} = -\hat{\boldsymbol{f}}_{xi+\frac{1}{2}}. \end{cases} \tag{12}$$

With spatial discretization given in (12), the semi-discrete equations are then solved using the explicit Runge-Kutta method [17,19]. It is noted that as the values at the cell interfaces are shared by the two neighboring cells, either the first or the third equation needs to be solved with the second equation in (12).

The MCV scheme can be straightforwardly extended to multi-dimensions for structured grids. The one-dimensional formulation given above can be applied in multi-dimensional problems by sweeping the different directions respectively. The numerical procedure is described in detail in [10].

2.2 A MCV scheme with TVD limiter

A three-point MCV scheme with TVD slope limiter was introduced in [21], which is also adopted in this study as an auxiliary spatial reconstruction profile in the present numerical formulation for a new high-order non-oscillatory MCV scheme.

Based on the basic idea proposed in [25], an additional constraint condition, i.e. the slope at the cell center, is introduced when building the spatial reconstruction of the dependent variable. Within cell $\mathcal{C}_i$, a cubic polynomial $\boldsymbol{Q}_i^{TVD}(x)$ is built using following conditions as

$$\begin{cases} \boldsymbol{Q}_i^{TVD}(x_{i1}) = \boldsymbol{q}_{i1}, \\ \boldsymbol{Q}_i^{TVD}(x_{i2}) = \boldsymbol{q}_{i2}, \\ \boldsymbol{Q}_i^{TVD}(x_{i3}) = \boldsymbol{q}_{i3}, \\ \boldsymbol{Q}_{xi}^{TVD}(x_{i2}) = \boldsymbol{d}_i, \end{cases} \tag{13}$$

where $\boldsymbol{q}_{i1}$, $\boldsymbol{q}_{i2}$ and $\boldsymbol{q}_{i3}$ are the known local DOFs and $\boldsymbol{d}_i$ is a parameter which can be used to adjust the numerical properties of the resulted scheme. By "TVD", we mean that the slope $\boldsymbol{d}_i$ is approximated by a TVD slope limiter as shown next.

The condition on the slope at the cell center plays a key role in the resulting scheme, which can be obtained by different algorithms to design the schemes with desired numerical properties [25,1].

To avoid the non-physical oscillations around the discontinuities, a minmod TVD slope limiter can be adopted as

$$\boldsymbol{d}_i = \text{minmod}\left(\boldsymbol{d}_l, \boldsymbol{d}_c, \boldsymbol{d}_r\right), \tag{14}$$

where

$$\begin{aligned} \boldsymbol{d}_l = 2.0\frac{\boldsymbol{q}_{i2} - \boldsymbol{q}_{i-1,2}}{\Delta x}, \quad \boldsymbol{d}_r = 2.0\frac{\boldsymbol{q}_{i+1,2} - \boldsymbol{q}_{i,2}}{\Delta x}, \\ \boldsymbol{d}_c = \frac{-\frac{4}{3}\boldsymbol{q}_{i1} + \frac{1}{6}\boldsymbol{q}_{i-1,2} + \frac{4}{3}\boldsymbol{q}_{i3} - \frac{1}{6}\boldsymbol{q}_{i+1,2}}{\Delta x}, \end{aligned} \tag{15}$$

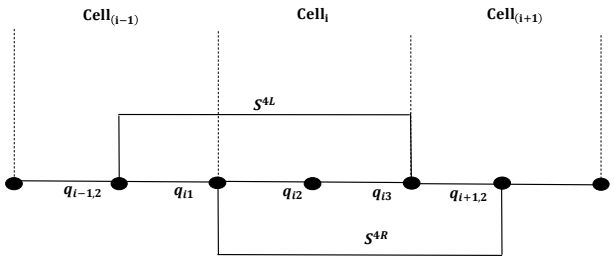

Fig. 1 Stencils for spatial reconstruction.

and

$$\text{minmod}\,(a,b,c) = \begin{cases} s \times \min(|a|,|b|,|c|) & \text{if } s = \text{sign}(a) = \text{sign}(b) = \text{sign}(c), \\ 0 & \text{otherwise.} \end{cases} \tag{16}$$

With spatial reconstruction $\boldsymbol{Q}_i^{TVD}(x)$ for the physical fields, the resulting scheme is non-oscillatory but at most of second-order accuracy even in the smooth areas. It should be notified that by replacing $\boldsymbol{Q}_{i-1}(x)$ and $\boldsymbol{Q}_i(x)$ with $\boldsymbol{Q}_{i-1}^{TVD}(x)$ and $\boldsymbol{Q}_i^{TVD}(x)$ in (10) the derivatives of the flux and thus the numerical solution will change, while the evolution equations to update the DOFs remain the same in form as (12). Hereafter, we denote the corresponding scheme as MCV3-TVD scheme. The numerical formulations of MCV3-TVD is completely same as MCV3 scheme shown above, except that the polynomial $\boldsymbol{Q}_i^{TVD}(x)$ is used in (10) instead of Lagrangian polynomial $\boldsymbol{Q}_i(x)$ through (6).

Different from the limiting procedure adopting in the original MCV scheme [10], DOFs defined at the cell interface are always shared by the two neighboring cells in the current study. As a result, the computation becomes more efficient regarding to both memory requirement and CPU cost as discussed in [12].

2.3 A non-oscillatory MCV scheme with boundary gradient switching

In this subsection, we further develop a non-oscillatory scheme using the MCV framework, which doesn't lose the original accuracy in smooth areas.

Following the work in [13], the cubic interpolation polynomial of dependent variable can be obtained by adopting the DOFs in left and right cells directly, instead of using the slope at cell center as an additional condition. As shown in Fig. 1, two stencils can be used for the reconstruction in cell $\mathcal{C}_i$, i.e. $\mathcal{S}^{4L}$ including the pointwise values at x_{i-1}, $x_{i-\frac{1}{2}}$, x_i and $x_{i+\frac{1}{2}}$ and $\mathcal{S}^{4R}$ including the pointwise values at $x_{i-\frac{1}{2}}$, x_i, $x_{i+\frac{1}{2}}$ and x_{i+1}.

Using stencil $\mathcal{S}^{4L}$, a cubic polynomial $\boldsymbol{Q}_i^{4L}$ in cell $\mathcal{C}_i$ is built with the conditions as

$$\begin{cases} \boldsymbol{Q}_i^{4L}\left(x_{i-1}\right)=\boldsymbol{q}_{i-1,2}, \\ \boldsymbol{Q}_i^{4L}\left(x_{i-\frac{1}{2}}\right)=\boldsymbol{q}_{i1}, \\ \boldsymbol{Q}_i^{4L}\left(x_i\right)=\boldsymbol{q}_{i2}, \\ \boldsymbol{Q}_i^{4L}\left(x_{i+\frac{1}{2}}\right)=\boldsymbol{q}_{i3}. \end{cases} \tag{17}$$

Similarly, another cubic polynomial $\boldsymbol{Q}_i^{4R}$ is obtained by using stencil $\mathcal{S}^{4R}$ as

$$\begin{cases} \boldsymbol{Q}_i^{4R}\left(x_{i-\frac{1}{2}}\right)=\boldsymbol{q}_{i1}, \\ \boldsymbol{Q}_i^{4R}\left(x_i\right)=\boldsymbol{q}_{i2}, \\ \boldsymbol{Q}_i^{4R}\left(x_{i+\frac{1}{2}}\right)=\boldsymbol{q}_{i3}, \\ \boldsymbol{Q}_i^{4R}\left(x_{i+1}\right)=\boldsymbol{q}_{i+1,2}. \end{cases} \tag{18}$$

Analogous to the MCV3-TVD scheme, substituting the spatial reconstruction $\boldsymbol{Q}_i\left(x\right)$ in subsection 2.1 with $\boldsymbol{Q}_i^{4L}$ or $\boldsymbol{Q}_i^{4R}$, and using the evolution equations (12) to update the DOFs, we get other two new schemes of fourth-order accuracy. We denote the scheme using $\boldsymbol{Q}_i^{4L}\left(x\right)$ for reconstruction as MCV3-4L and one with $\boldsymbol{Q}_i^{4R}\left(x\right)$ as MCV3-4R, hereafter. However, without any limiting both MCV3-4L and MCV3-4R schemes will generate spurious numerical oscillations around the discontinuities, which even leads to the blow-up of computations when solving problems with shock waves.

In this study, we propose a boundary gradient switching (BGS) algorithm considering the variation-minimization principle, which adopts the basic idea in ENO method [6] and is used to choose the smoother spatial reconstruction profile between $\boldsymbol{Q}_i^{4L}$ and $\boldsymbol{Q}_i^{4R}$ in comparison with $\boldsymbol{Q}_i^{TVD}$. This scheme is referred to as MCV3-BGS scheme, which effectively suppresses non-physical oscillations in numerical solutions while realizing high-order accuracy in smooth region. The numerical formulation given in (10) is then recast into

$$\begin{cases} \hat{\boldsymbol{f}}_{xi-\frac{1}{2}}^{-}=\boldsymbol{A}_{i-\frac{1}{2}}\mathrm{BGS}\left[\left(\frac{\partial \boldsymbol{Q}_{i-1}(x)}{\partial x}\right)_{i-\frac{1}{2}}\right], \\ \hat{\boldsymbol{f}}_{xi-\frac{1}{2}}^{+}=\boldsymbol{A}_{i-\frac{1}{2}}\mathrm{BGS}\left[\left(\frac{\partial \boldsymbol{Q}_{i}(x)}{\partial x}\right)_{i-\frac{1}{2}}\right], \end{cases} \tag{19}$$

with $\mathrm{BGS}\left[\left(\frac{\partial \boldsymbol{Q}_i(x)}{\partial x}\right)_{i-\frac{1}{2}}\right]$ being calculated by

$$\mathrm{BGS}\left[\left(\frac{\partial \boldsymbol{Q}_i\left(x\right)}{\partial x}\right)_{i-\frac{1}{2}}\right]=\begin{cases} \mathrm{dmin}\left(\boldsymbol{d}_1,\boldsymbol{d}_2\right) \text{ if } \mathrm{sign}\left(\boldsymbol{d}_1\right)=\mathrm{sign}\left(\boldsymbol{d}_2\right)=\mathrm{sign}\left(\boldsymbol{d}_3\right), \\ \boldsymbol{d}_1 \text{ only if } \mathrm{sign}\left(\boldsymbol{d}_1\right)=\mathrm{sign}\left(\boldsymbol{d}_3\right), \\ \boldsymbol{d}_2 \text{ only if } \mathrm{sign}\left(\boldsymbol{d}_2\right)=\mathrm{sign}\left(\boldsymbol{d}_3\right), \\ \mathrm{absmin}\left(\boldsymbol{d}_1,\boldsymbol{d}_2\right) \text{ otherwise}, \end{cases} \tag{20}$$

where

$$\begin{cases} \boldsymbol{d}_1=\left(\frac{\partial \boldsymbol{Q}_i^{4L}(x)}{\partial x}\right)_{i-\frac{1}{2}}, \\ \boldsymbol{d}_2=\left(\frac{\partial \boldsymbol{Q}_i^{4R}(x)}{\partial x}\right)_{i-\frac{1}{2}}, \\ \boldsymbol{d}_3=\left(\frac{\partial \boldsymbol{Q}_i^{TVD}(x)}{\partial x}\right)_{i-\frac{1}{2}}, \end{cases} \tag{21}$$

and dmin is the variation diminishing function, absmin is the absolute minimum function defined by

$$\mathrm{dmin}\left(\boldsymbol{d}_1, \boldsymbol{d}_2\right) = \begin{cases} \boldsymbol{d}_1 & \text{if} \quad |\boldsymbol{d}_1 - \boldsymbol{d}_3| < |\boldsymbol{d}_2 - \boldsymbol{d}_3|, \\ \boldsymbol{d}_2 & \text{otherwise}, \end{cases} \tag{22}$$

$$\mathrm{absmin}\left(\boldsymbol{d}_1, \boldsymbol{d}_2\right) = \begin{cases} \boldsymbol{d}_1 & \text{if} \quad |\boldsymbol{d}_1| < |\boldsymbol{d}_2|, \\ \boldsymbol{d}_2 & \text{otherwise}. \end{cases} \tag{23}$$

With this BGS algorithm, the smoother approximation of derivative of flux function is adopted during computations to remove the non-physical oscillations as shown in the benchmark tests in the next section. Meanwhile, the BGS processing doesn't degrade the accuracy of the proposed scheme since both MCV3-4L and MCV3-4R schemes are fourth-order accurate.

3 Tests and results

In this section, we verify the proposed MCV3-BGS scheme by simulating the widely-used benchmark tests of one- and two-dimensional hyperbolic conservation laws. The SSP Runge-Kutta method (SSPRK(5,4)) [19] is adopted in this study for time marching and the maximal allowable CFL number for computational stability is about 0.6.

3.1 One-dimensional linear advection equation

The one-dimensional advection equation with a constant speed is simulated. The governing equation is specified by $\boldsymbol{q} = \phi$ and $\boldsymbol{f}\left(\boldsymbol{q}\right) = \phi$ in (1) where ϕ is the advected field.

3.1.1 Advection of one-dimensional sine wave

This test is carried out on gradually refined grids to evaluate the convergence rate of the proposed scheme. The initial smooth distribution is given by

$$\phi\left(x, 0\right) = \sin\left(\pi x\right), \ x \in \left[-1, 1\right]. \tag{24}$$

The l_1 and l_∞ errors are defined as

$$l_1 = \sum_{i=1}^{I} \frac{|\phi_i^e - \phi_i^n|}{I}, \text{ and } l_\infty = max_{1 \le i \le I} |\phi_i^e - \phi_i^n|, \tag{25}$$

where ϕ^e and ϕ^n stand for exact and numerical solutions respectively.

We ran the computation for one period (at $t = 2.0$) and summarize the numerical errors and the convergence rates for MCV3-4L, MCV3-4R and MCV-BGS in Table 1. Compared with MCV3-4L and MCV3-4R schemes, the BGS algorithm does not make significant differences in convergence rate regarding to l_1 error for this test with smooth solution. MCV3-BGS scheme achieves the 4th-order accuracy regarding to l_1 error as expected. Error l_∞ of MCV3-BGS scheme shows a little slower convergence rate.

Table 1 Numerical errors and convergence rates of the 1D advection equation for sinusoidal profile distribution

	Grids	l_1 error	l_1 order	l_∞ error	l_∞ order
MCV3-4L	20	1.0441e-04	–	1.6298e-04	–
	40	6.5192e-06	4.00	1.0261e-05	3.99
	80	4.0899e-07	3.99	6.4196e-07	4.00
	160	2.5576e-08	4.00	4.0291e-08	3.99
	320	1.5990e-09	4.00	2.6706e-09	3.92
MCV3-4R	20	2.0007e-04	–	3.1091e-03	–
	40	1.3362e-05	3.90	2.0974e-04	3.89
	80	8.5350e-07	3.97	1.3405e-06	3.97
	160	5.3712e-08	3.99	8.4555e-08	3.99
	320	3.3652e-09	4.00	5.4692e-09	3.95
MCV3-BGS	20	1.7824e-04	–	5.5121e-04	–
	40	1.6697e-05	3.42	6.8212e-05	3.01
	80	1.1200e-06	3.80	6.0404e-06	3.50
	160	7.8740e-08	3.93	6.1734e-07	3.29
	320	4.9661e-09	3.99	5.2868e-08	3.55

3.1.2 Advection of one-dimensional square wave

In this test, the propagation of a square wave is simulated to check the ability of the proposed scheme to capture discontinuous solutions. The initial profile is

$$\phi(x,0) = \begin{cases} 1 \text{ if} |x| \leq 0.4, \\ 0 \text{ otherwise.} \end{cases} \tag{26}$$

Numerical experiment was carried out on the uniform grid with 200 cells. The numerical results using MCV3-4L and MCV3-4R are depicted in Fig. 2. The non-physical oscillations are obviously found in both results. Considering the ability of dealing with the discontinuity, MCV3-4R scheme performs better than MCV3-4L scheme though it gives smaller absolute errors for a smooth profile in the above case. It is noted that this observation is only for the case with a positive advection velocity. For a negative advection velocity, the spatial discretization is constructed using new stencils, which are symmetrical to those used here with respect to the cell boundary in line with the upwinding spirit.

The numerical result by MCV3-BGS scheme is shown in Fig. 3. The BGS algorithm always tends to choose the smoother spatial reconstruction between MCV3-4L and MCV3-4R schemes and the non-physical oscillations are effectively removed. Meanwhile, the numerical diffusion is controlled to a minimized extent, as the jumps are well resolved by MCV3-BGS scheme with a more compact thickness in comparison with other existing schemes.

3.1.3 Advection of one-dimensional complex wave

To examine the performance of the proposed scheme in solving profiles of different smoothness, we further simulated the propagation of a complex wave [11], which includes both discontinuous and smooth solutions. The initial distribution of the

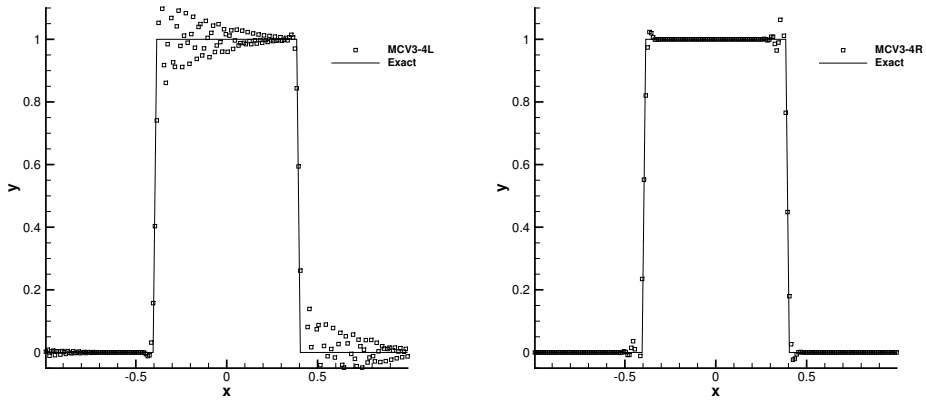

Fig. 2 Numerical results of 1D advection of a square wave by MCV3-4L scheme (left panel) and MCV3-4R (right panel) with 200 cells after one period.

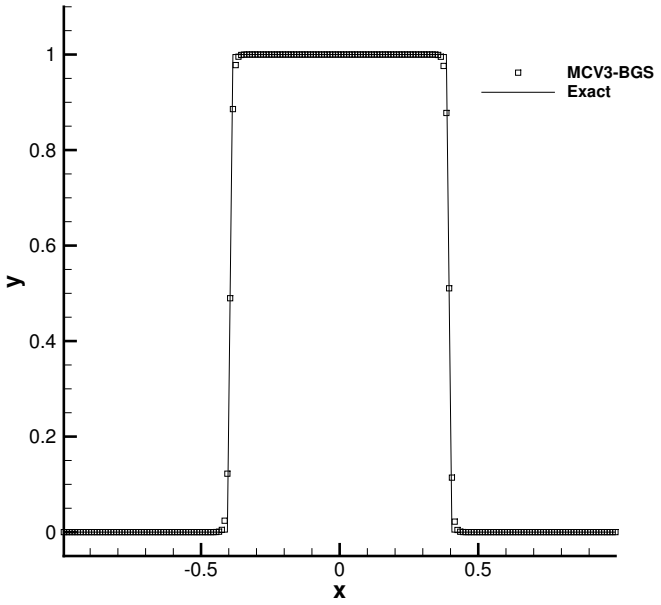

Fig. 3 Numerical result of 1D advection of a square wave by MCV3-BGS scheme with 200 cells after one period.

advected field is

$$\phi(x,0)=\begin{cases}\frac{1}{6}\left[G(x,\beta,z-\delta)+G(x,\beta,z+\delta)+4G(x,\beta,z)\right] \text{ if } |x+0.7|\leq 0.1,\\ 1 \text{ if } |x+0.3|\leq 0.1,\\ 1-|10(x-0.1)| \text{ if } |x-0.1|\leq 0.1,\\ \frac{1}{6}\left[F(x,\alpha,a-\delta)+F(x,\alpha,a+\delta)+4F(x,\alpha,a)\right] \text{ if } |x-0.5|\leq 0.1,\\ 0 \text{ otherwise,}\end{cases}, \tag{27}$$

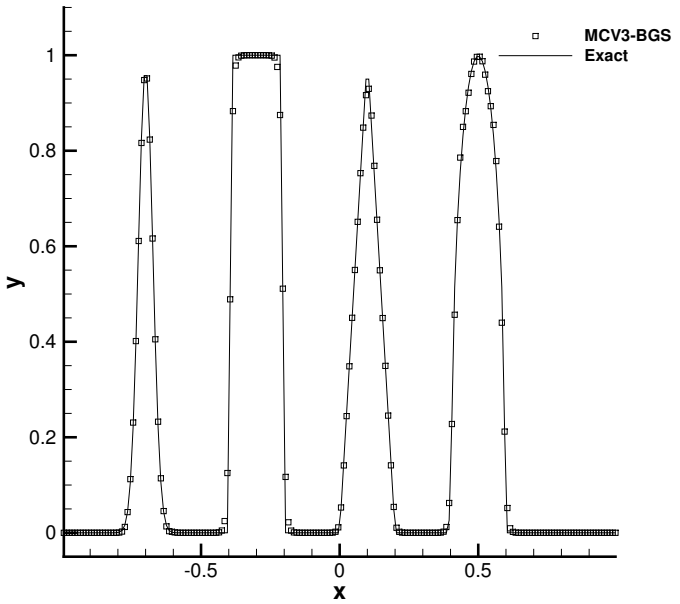

Fig. 4 Numerical results of 1D advection of complex wave with 200 cells after one period.

where functions F and G are defined as

$$G\left(x,\beta,z\right)=\exp\left[-\beta\left(x-z\right)^{2}\right],\ F\left(x,\alpha,a\right)=\sqrt{\max\left[1-\alpha^{2}\left(x-a\right)^{2},0\right]}, \quad (28)$$

and the coefficients are

$$a=0.5,\ z=0.7,\ \delta=0.005,\ \alpha=10.0,\ \beta=\log_{2}\left(36\delta^{2}\right). \quad (29)$$

The numerical result after one period of computation on a 200-cell mesh is plotted in Fig.4. It shows that the discontinuities are sharply represented without visible oscillations, while the smooth extremes are well preserved due to the high-order accuracy of the proposed scheme.

3.2 One-dimensional inviscid Burgers' equation

The one-dimensional inviscid Burgers' equation is obtained by specifying $\boldsymbol{q}=u$ and $\boldsymbol{f}\left(\boldsymbol{q}\right)=\frac{u^{2}}{2}$ in (1). The shock will develop even from a smooth initial condition with this non-linear equation.

For the inviscid Burgers' equation, the derivative Riemann problem is computed by a pure upwind scheme at the cell boundary $x_{i-\frac{1}{2}}$ and (9) is written as [10]

$$\hat{f}_{xi-\frac{1}{2}}=\frac{1}{2}\left[\hat{f}^{-}_{xi-\frac{1}{2}}+\hat{f}^{+}_{xi-\frac{1}{2}}-\mathrm{sign}\left(\alpha_{i-\frac{1}{2}}\right)\left(\hat{f}^{-}_{xi-\frac{1}{2}}+\hat{f}^{+}_{xi-\frac{1}{2}}\right)\right], \quad (30)$$

Table 2 Numerical errors and convergence rates of the 1D inviscid Burgers' equation

Grid	l_1 error	l_1 order	l_∞ error	l_∞ order
40	6.7402e-05	-	1.5536e-03	-
80	5.3180e-06	3.66	1.8428e-04	3.08
160	3.8335e-07	3.79	1.8069e-05	3.35
320	2.5456e-08	3.91	1.6796e-06	3.43
640	1.7071e-09	3.88	1.5114e-07	3.47

where $\alpha_{i+\frac{1}{2}} = \frac{1}{2}\left(\overline{{}^{V}u}_{i-1} + \overline{{}^{V}u}_{i}\right)$ and $\overline{{}^{V}u}_{i}$ is the VIA moment for u in cell $\mathcal{C}_i$.

The BGS algorithm is performed in terms of the flux function in simulating the Burgers' equation. The spatial reconstructions (13) for MCV3-TVD, (17) for MCV3-4L and (18) for MCV3-4R are implemented in terms of flux function rather than the dependent variable. The derivatives of flux functions in (19) is computed by

$$\hat{\boldsymbol{f}}^{-}_{xi-\frac{1}{2}} = \mathrm{BGS}\left[\left(\frac{\partial \boldsymbol{F}_{i-1}(x)}{\partial x}\right)_{i-\frac{1}{2}}\right] \text{ and } \hat{\boldsymbol{f}}^{+}_{xi-\frac{1}{2}} = \mathrm{BGS}\left[\left(\frac{\partial \boldsymbol{F}_{i}(x)}{\partial x}\right)_{i-\frac{1}{2}}\right], \quad (31)$$

where $\boldsymbol{F}$ represents the polynomial for flux function and the operator BGS is specified as in (20) by replacing $\boldsymbol{Q}$ with $\boldsymbol{F}$.

3.2.1 Accuracy test of 1D inviscid Burgers' equation

To test the convergence rate of the proposed scheme for a non-linear equation, we solve inviscid Burgers' equation with initial condition $u(x,0) = 0.5 + \sin(\pi x)$. The exact solution profile will remain smooth until $t = 1.0/\pi$ before producing a moving shock and a rarefaction wave. The computation is evolved to $t = 0.5/\pi$ to calculate the l_1 and l_∞ errors which have been summered in Table 2. We can see that the proposed MCV3-BGS scheme converges nearly with a 4th-order accuracy regarding to l_1 order for this nonlinear test.

3.2.2 Shock capturing test of 1D inviscid Burgers' equation

We solve the above equation with a smooth initial condition as

$$u(x,0) = 0.5 + 0.4\cos(2\pi x). \quad (32)$$

The time step is set as $\Delta t = 0.2\Delta x$ in this test. The result calculated on a uniform grid with 100 cells at $t = 1$ is given in Fig. 5.

Shock can be observed in the numerical result. With the BGS algorithm, the shock wave is well resolved (within two cells) without visible non-physical oscillation. The numerical result verified the performance of the proposed scheme in solving the non-linear problem.

3.3 One-dimensional Euler equations

The one-dimensional Euler equations are specified as

$$\boldsymbol{q} = [\rho, \rho u, E]^T, \ \boldsymbol{f}(\boldsymbol{q}) = \left[\rho u, \rho u^2 + p, u(E+p)\right]^T, \quad (33)$$

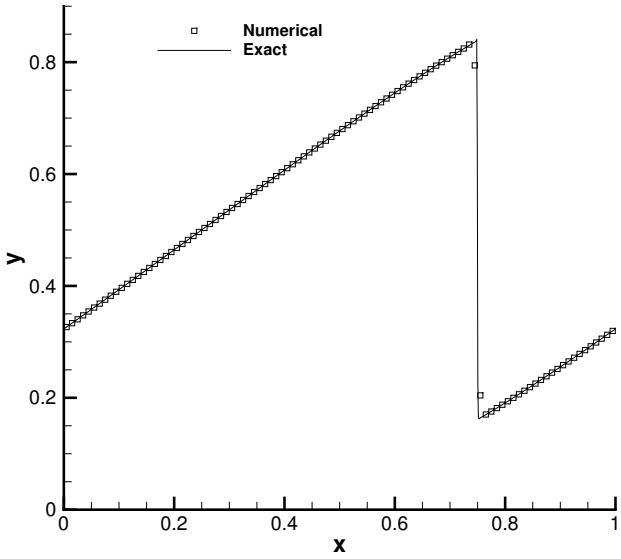

Fig. 5 Numerical results of Burgers' equation at t=1 with 100 cells.

where ρ is the density, u the velocity, p the pressure and E the total energy. The equation of state of ideal gas is $E = \frac{p}{\gamma-1} + \frac{1}{2}\rho u^2$ with $\gamma = 1.4$.

The Jacobian matrix $\boldsymbol{A}$ is calculated following [9] as

$$\boldsymbol{A}_{i-\frac{1}{2}} = \frac{1}{2}(\bar{\boldsymbol{A}}_{i-\frac{1}{2}} + \tilde{\boldsymbol{A}}_{i-\frac{1}{2}}), \tag{34}$$

where $\bar{\boldsymbol{A}}_{i-\frac{1}{2}}$ is the Roe-averaged Jacobian matrix computed from the VIA moments of dependent variables in cells $\mathcal{C}_{i-1}$ and $\mathcal{C}_i$ and $\tilde{\boldsymbol{A}}_{i-\frac{1}{2}}$ is obtained directly from the point values of the physical variables at the cell interface.

For Euler equations, the BGS operation is applied to the characteristic variables and the solution procedure can be referred to [21]. Following the studies in [8], the time step in the test cases for one-dimensional Euler equations is simply set to be $\Delta t = 0.1\Delta x$ unless a special statement is made.

3.3.1 Accuracy test for 1D Euler equations

We compute the propagation of smooth density perturbation [14] to check the convergence rate of the proposed scheme. The constant pressure and velocity are specified as $p_0 = 1.0$ and $u_0 = 1.0$ initially. A smooth distribution of density field is given as $\rho_0 = 1.0 + 0.2\sin(\pi x)$. The computational domain is $x \in [0, 2]$ with periodic boundary condition. The l_1 and l_∞ errors and accuracy orders are measured at $t = 2.0$ shown in Table 3. Similar orders are obtained as those for 1D advection equation and Burgers' equation.

Table 3 Numerical errors and convergence rates of 1D Euler system

Grid	l_1 error	l_1 order	l_∞ error	l_∞ order
20	3.4584e-05	-	5.3566e-05	-
40	2.9814e-06	3.54	6.3772e-06	3.07
80	2.0704e-07	3.85	5.4503e-07	3.55
160	1.3621e-08	3.93	5.0466e-08	3.43
320	8.7315e-10	3.96	4.1708e-09	3.60

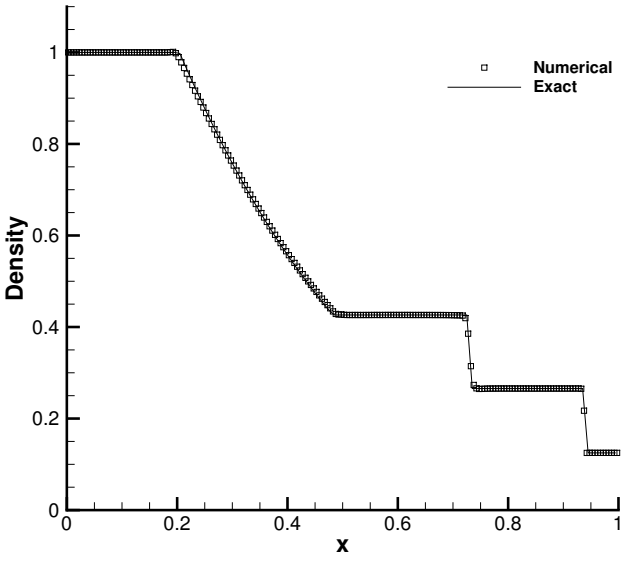

Fig. 6 Numerical result for density field of Sod's problem at t = 0.25 with 200 cells.

3.3.2 Sod's problem

For this problem, the initial distribution is specified as [18]

$$(\rho_0,\ u_0,\ p_0) = \begin{cases} (1,\ 0,\ 1) \text{ if } 0 \le x \le 0.5, \\ (0.125,\ 0,\ 0.1) \text{ otherwise.} \end{cases} \tag{35}$$

The computation is carried out with 200 uniform cells and the model is integrated up to $t = 0.25$. The numerical result is presented in Fig. 6. The current method shows better results in comparison with most existing methods.

3.3.3 Lax's problem

As one of benchmark test for shock tube problem, Lax problem is used to check the ability of the numerical schemes to capture relatively strong shock [17]. The initial profile is

$$(\rho_0,\ u_0,\ p_0) = \begin{cases} (0.445,\ 0.698,\ 3.528) \text{ if } 0 \le x \le 0.5, \\ (0.5,\ 0,\ 0.571) \text{ otherwise.} \end{cases} \tag{36}$$

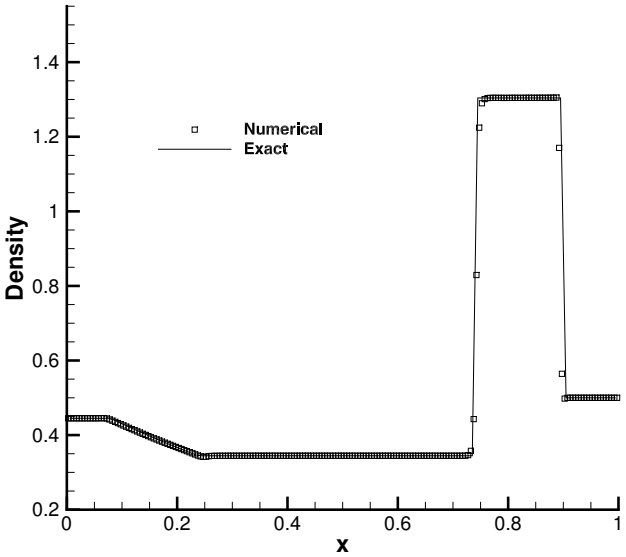

Fig. 7 Numerical result for density field of Lax's problem at t = 0.16 with 200 cells.

With the same number of cells as in the previous case, the numerical results at $t = 0.16$ are shown in Fig. 7. We can see that MCV3-BGS scheme can effectively suppress the oscillations near the shock and accurately resolve both contact discontinuity and expansion wave due to the less numerical diffusion.

3.3.4 Shock-turbulence interaction

As in [16], interactions between a shock wave and wavy perturbations are simulated with the following initial condition

$$(\rho_0,\ u_0,\ p_0) = \begin{cases} (3.857148,\ 2.629369,\ 10.333333) \ \text{if } 0 \le x \le 1, \\ (1 + 0.2\sin(5x - 5),\ 0,\ 1) \ \text{otherwise.} \end{cases} \tag{37}$$

In this case, the shock moves towards the right and then interacts with a wave chain in density. Both shock and complex smooth structures exist in the solution. So, the numerical scheme is required to be not only capable of capturing the shock but also accurate enough to resolve the complex flow in smooth region with minimized numerical dissipation. The numerical results of MCV3-BGS with 200 mesh cells at $t = 1.8$ are shown in Fig. 8. The reference solution plotted by the solid line is computed by the classical fifth-order WENO scheme [11] with 2000 mesh cells.It can be seen from the numerical results that the present scheme can reproduce the shocks without spurious oscillations and accurately capture density perturbations.

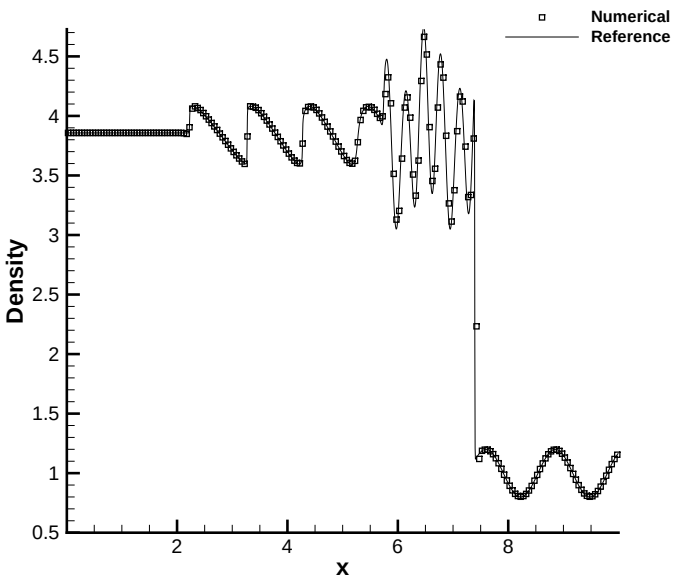

Fig. 8 Numerical result for density field of shock-turbulence interaction at $t = 1.8$ with 200 cells.

3.3.5 Two interacting blast waves

We also computed two interacting blast waves suggested in [24]. Multiple interactions of strong shocks and rarefaction waves are included in this test problem.The initial distribution has uniform density of $\rho = 1$ and velocity of zero. The difference exists in the distribution of pressure as

$$p_0 = \begin{cases} 1000 \text{ if } 0 \le x \le 0.1, \\ 0.01 \text{ if } 0.1 < x \le 0.9, \\ 100 \text{ otherwise.} \end{cases} \tag{38}$$

Reflective boundary conditions are imposed at the two ends of computational domain. Two blast waves are generated by the initial jumps and interact each other violently. Strong shocks, contact discontinuities and expansion fans are generated and cause further interactions. The number of the mesh cells of 400 is used in this test. Here we set $\Delta t = 0.02\Delta x$ due to strong shock.

We depict the numerical solution of density at $t = 0.038$ in Fig. 9, where the reference solution is computed by the classical fifth-order WENO scheme [11] with 2000 mesh cells.

Again, the numerical results of MCV3-BGS scheme are among the best ever reported in the literature.

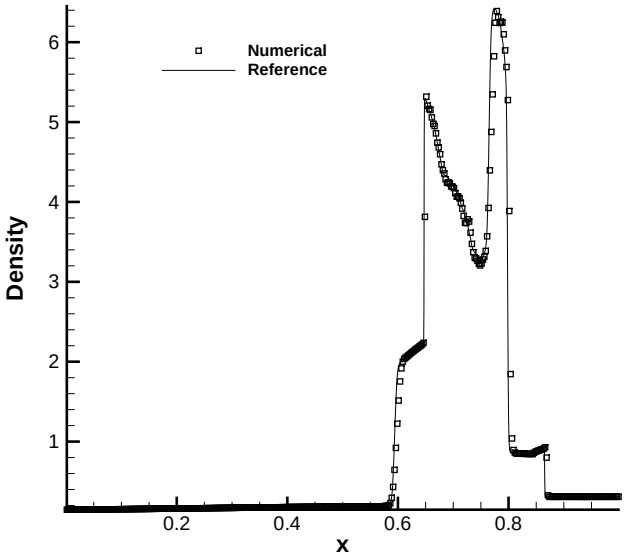

Fig. 9 Numerical result for density field of two interacting blast waves at t = 0.038 with 400 cells.

3.4 Two-dimensional linear advection equation

The two-dimensional hyperbolic system is written in Cartesian grid as

$$\frac{\partial \boldsymbol{q}}{\partial t} + \frac{\partial \boldsymbol{e}(\boldsymbol{q})}{\partial x} + \frac{\partial \boldsymbol{f}(\boldsymbol{q})}{\partial y} = 0, \tag{39}$$

where $\boldsymbol{q}$ is the vector of dependent variables, $\boldsymbol{e}(\boldsymbol{q})$ and $\boldsymbol{f}(\boldsymbol{q})$ the vectors of flux functions in x- and y-directions, respectively.

The two-dimensional linear advection equation is specified by $\boldsymbol{q} = \phi$, $\boldsymbol{e}(\boldsymbol{q}) = u\phi$ and $\boldsymbol{f}(\boldsymbol{q}) = v\phi$ in (39) where (u, v) is the velocity vector.

3.4.1 Advection of two-dimensional sine wave

The convergence rate of the proposed scheme are checked in this two-dimensional advection case by running a smooth sine wave on gradually refined grids. The initial condition is given in computational domain $[-1, 1] \times [-1, 1]$ as

$$\phi(x, y, 0) = \sin[\pi(x + y)]. \tag{40}$$

The uniform velocity is set as $(u, v) = (1, 1)$. The normalized error l_1 at $t = 2$ are shown in Table 4.

The numerical results verify the expected convergence rate of 4th-order regarding to l_1 error of the proposed MCV-BGS scheme in two-dimensional case as well.

Table 4 Numerical errors and convergence rates of the 2D advection equation

Grid	l_1 error	l_1 order	l_∞ error	l_∞ order
10	3.9644e-03	-	9.4769e-03	-
20	4.6692e-04	3.08	1.2102e-03	2.97
40	3.6717e-05	3.67	1.1372e-04	3.41
80	2.6815e-06	3.78	1.0026e-05	3.50
160	1.7166e-07	3.97	8.6287e-07	3.54

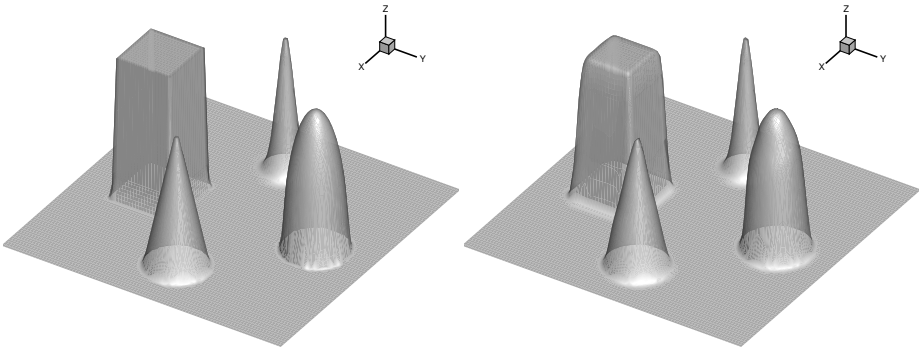

Fig. 10 Numerical result of 2D rotation of complex wave after one period with 100×100 cells. shown are initial profile (left panel) and numerical result (right panel).

3.4.2 Rotation of two-dimensional complex wave

We extend the one-dimensional Jiang and Shu's problem [11] to two-dimensional case with a rotational velocity field defined by $(u, v) = (-2\pi x, 2\pi y)$. The computational domain is $[-1, 1] \times [-1, 1]$. The initial distribution is defined by

$$u(x, y, 0) = \begin{cases} \frac{1}{6}\left[G(r_1 + \delta, \beta) + G(r_1 - \delta, \beta) + 4G(r_1, \beta)\right] \text{ if } r_1 \leq 0.2, \\ 1 \text{ if } |x| \leq 0.2, -0.7 \leq y \leq -0.3, \\ 1 - 5r_2 \text{ if } r_2 \leq 0.2, \\ \frac{1}{6}[F(r_3 + \delta, \alpha) + F(r_3 - \delta, \alpha) + 4F(r_3, \alpha)] \text{ if } |r_3| \leq 0.2, \\ 0 \text{ otherwise}, \end{cases} \tag{41}$$

where

$$r_1 = \sqrt{(x + 0.6)^2 + y^2},\ r_2 = \sqrt{(x - 0.6)^2 + y^2},\ r_3 = \sqrt{x^2 + (y - 0.6)^2}, \tag{42}$$

$G(r, \beta) = \exp\left(-\beta r^2\right)$, $F(r, \alpha) = \sqrt{\max\left(1 - \alpha^2 r^2, 0\right)}$ and the coefficients are set to be $\delta = 0.01$, $\alpha = 5$ and $\beta = log_2\left(36\delta^2\right)$.

The model runs up to $t = 1$ (after one period) with 100×100 uniform cells.The initial profile and numerical result are shown in Fig. 10. There are no visible oscillation around the discontinuities and all structures including the smooth extremes are adequately resolved compared with the initial condition. Furthermore, we didn't find the noticeable deformation of the distribution of the advected field in this two-dimensional case.

Table 5 Numerical errors and convergence rates of 2D Euler system

Grid	l_1 error	l_1 order	l_∞ error	l_∞ order
10	7.8337e-04	-	1.7825e-03	-
20	9.3258e-05	3.07	2.2563e-04	2.98
40	7.4606e-06	3.22	1.9792e-05	3.51
80	5.4062e-07	3.79	1.6773e-06	3.56
160	3.5283e-08	3.94	1.4336e-07	3.55

3.5 Two-dimensional Euler equations

In (39), two-dimensional Euler equations have the form of

$$\begin{cases} \boldsymbol{q} = [\rho, \rho u, \rho v, E]^T, \\ \boldsymbol{e}(\boldsymbol{q}) = \left[\rho u, \rho u^2 + p, \rho uv, u(E+p)\right]^T, \\ \boldsymbol{f}(\boldsymbol{q}) = \left[\rho v, \rho uv, \rho v^2 + p, v(E+p)\right]^T, \end{cases} \tag{43}$$

where u and v are velocity components in x- and y-directions. Due to the regularity of the mesh, we can implement the one-dimensional formulation to each directions directly. The expressions of Jacobian matrices $\boldsymbol{A} = (\partial \boldsymbol{e}/\partial \boldsymbol{q})$ for x direction and $\boldsymbol{B} = (\partial \boldsymbol{f}/\partial \boldsymbol{q})$ for y direction can be found in text books, e.g. [5]. In practice, $\boldsymbol{A}$ are calculated along the line segments as the equation (34) in which Jacobian matrix $\boldsymbol{A}$ are an arithmetic average between $\bar{\boldsymbol{A}}$ and $\tilde{\boldsymbol{A}}$, where $\bar{\boldsymbol{A}}$ is the Roe-averaged Jacobian matrix computed from the VIA values of two neighboring cells along line segments while $\tilde{\boldsymbol{A}}$ is obtained directly from the point values. The same applies to matrix $\boldsymbol{B}$.

3.5.1 Accuracy test for 2D Euler equations

The propagation of the density perturbation in 2D case is specified with $\rho_0 = 1.0 + 0.2\sin[\pi(x+y)]$, $(u_0, v_0) = (0.7, 0.3)$ and $p_0 = 1.0$. The computational domain is $[-1,1] \times [-1,1]$ with periodic boundary condition. The l_1 and l_∞ errors and accuracy orders are measured at $t = 2.0$ shown in Table 5. The expected accuracy orders of the proposed scheme are achieved for solving 2D Euler equations.

3.5.2 Two-dimensional explosion

An axi-symmetric two dimensional explosion problem as described in [22] is simulated. As the initial condition, a region inside a circle of radius $R = 0.4$ is set with high pressure and density as

$$(\rho_0,\ u_0,\ v_0,\ p_0) = \begin{cases} (1.0,\ 0.0,\ 0.0,\ 1.0) & \text{if } r \le R, \\ (0.125,\ 0.0,\ 0.0,\ 0.1) & \text{otherwise}, \end{cases} \tag{44}$$

where $r = \sqrt{x^2 + y^2}$ is distance to the center of the computational domain.

As time goes on, the fluid inside the circle will spread out and form a moving shock, a contact discontinuity and a rarefaction wave of cylindrical symmetry. The MCV-BGS model runs up to $t = 0.25$ on a grid with 200×200 uniform cells.The bird's-eye view of pressure distribution and the cut-off profile along radial direction

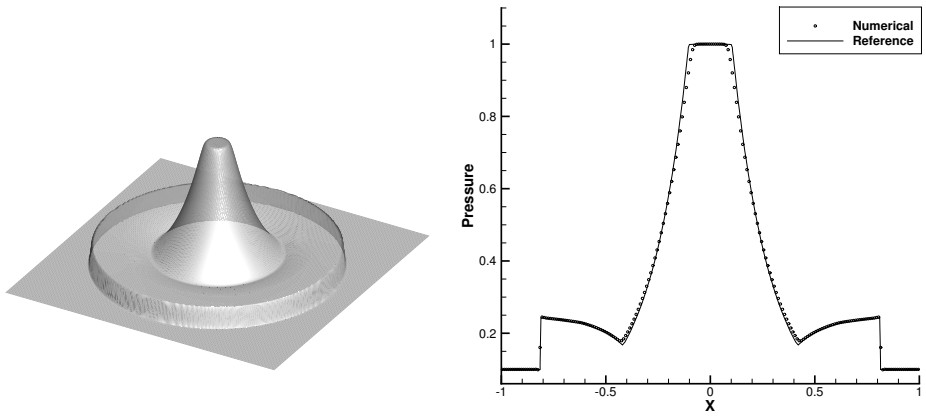

Fig. 11 Numerical result for pressure field of 2D explosion at t = 0.25 with 200×200 cells. Shown are bird's-eye view of pressure distribution (left panel) and cut-off profile along radial direction (right panel).

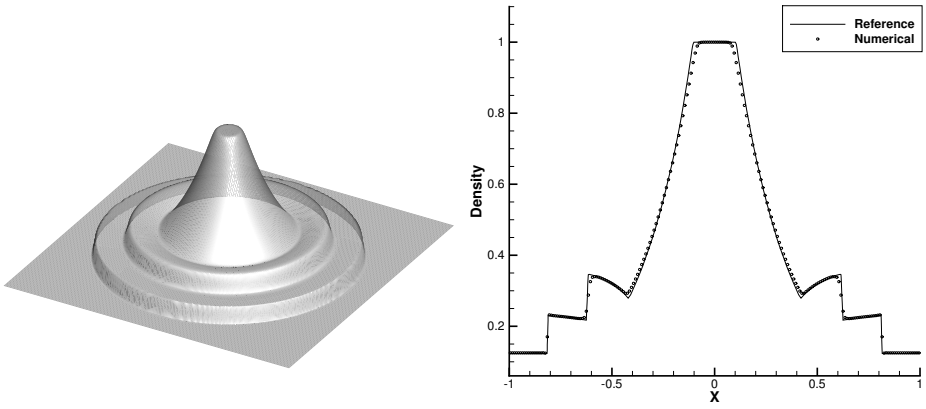

Fig. 12 Same as Fig. 11, but for density field.

are shown in Fig. 11. The corresponding numerical results of density are presented in Fig. 12.

It is observed from our numerical results that the MCV3-BGS scheme can accurately resolve the shock wave, contact discontinuity and rarefaction fan with adequate resolution. The symmetry of numerical solutions remain perfect, which demonstrates the less grid-dependency and high geometrical fidelity of the proposed scheme.

3.5.3 Double Mach reflection

A propagating planar shock, at $Ma = 10$ in hypersonic regime, reflected by 30° ramp is simulated in this case. It is well known that it is difficult for a numerical scheme to well resolve the very strong discontinuities and the rich small-scale structures developing with time at the same time [24]. The computational domain is $[0, 4] \times [0, 1]$. A right-moving Mach 10 shock is imposed with 60° angle relative

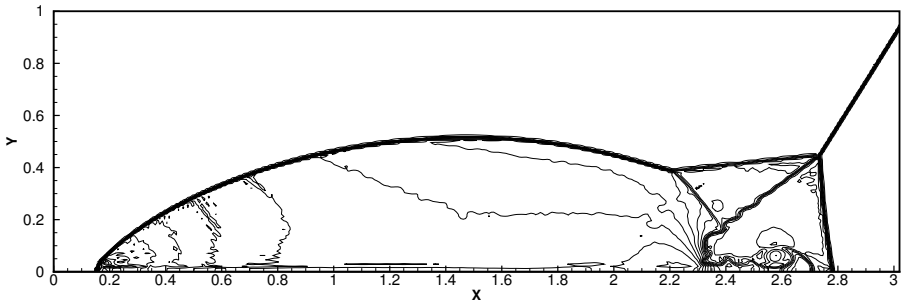

Fig. 13 Numerical result for density field of the double Mach reflection at $t = 0.2$ with 384×120 cells.

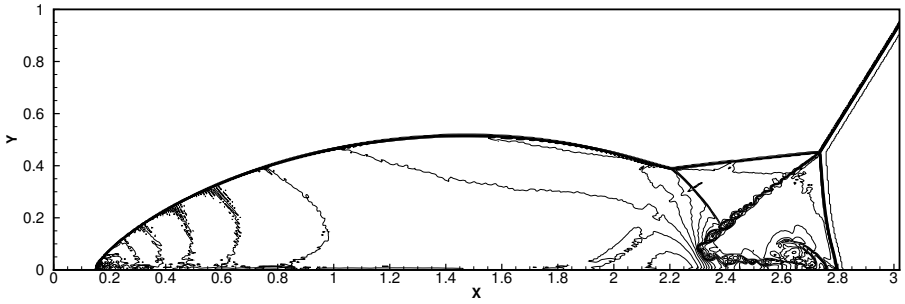

Fig. 14 Same as Fig. 13, but with 800×250 cells.

to x-axis. At the right boundary of the computational domain, the boundary condition is given by setting all gradients to be zero.

Two grid with different resolution are adopted to calculate this test. The contour plots of the numerical results of the density field at $t = 0.2$ are illustrated in Fig. 13 on coarse grid and Fig. 14 on fine one. The enlarged view of the vortex structures and instability along the slip lines are shown in Fig. 15. Both the strong discontinuities and the vortex structures are well resolved in the current results by MCV3-BGS scheme, which shows the well-controlled numerical dissipation in MCV3-BGS scheme.

3.6 A Mach 3 wind tunnel with a step

Simulation of Mach 3 wind tunnel with a step is one of the popular benchmark tests for verification of high-resolution schemes [24]. In this case, the computational domain is $[0, 3] \times [0, 1]$ and a step with height of 0.2 is located at $x = 0.6$. The inflow and outflow conditions are prescribed along the left and right boundaries and the rest are imposed with the reflective condition. The numerical tests are conducted with different spatial resolutions. As shown in Figs.16 and 17, the density field at $t = 4.0$ are depicted for the numerical results on grids of 480×160 and 960×320 respectively. It is observed that the shock waves and strong discontinuities are adequately resolved without the visible numerical oscillations. Meanwhile, the

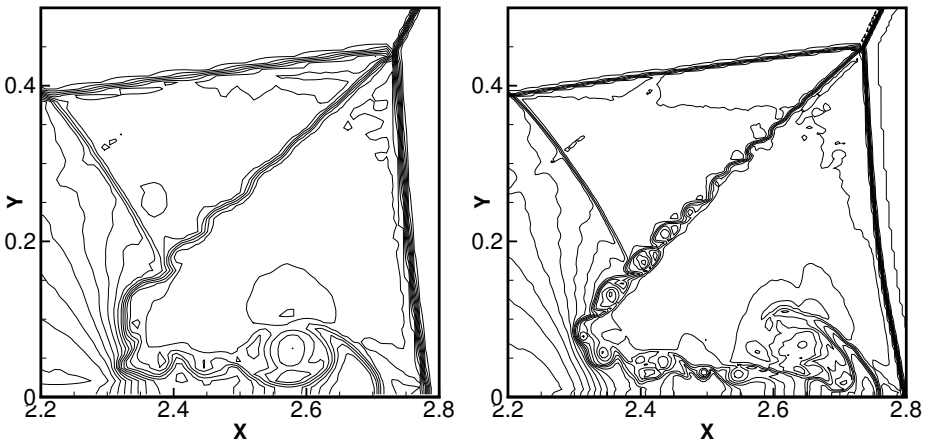

Fig. 15 Enlarged view of vortex structures and instability along the slip lines of double Mach reflection at t = 0.2 with 384 × 120 cells (left panel) and 800 × 250 cells (right panel).

numerical dissipation is also suppressed so that the vortical structures of acoustic waves are sufficiently captured. The proposed method can resolve the vortical structures better with fewer mesh cells in comparison with the original WENO scheme and its new variants reported in [4].

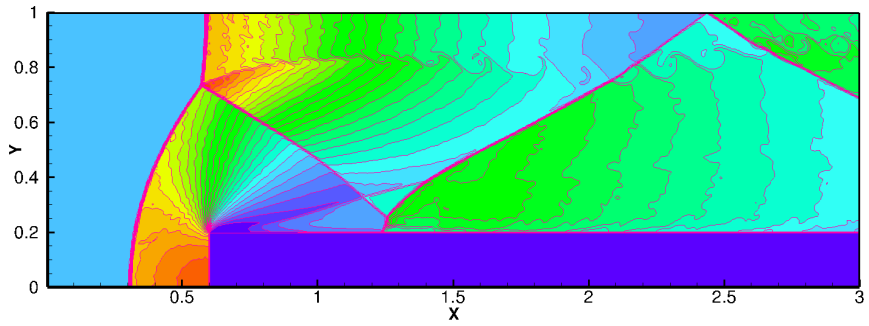

Fig. 16 Density contours for the Mach 3 wind tunnel with a step at $t = 4$ with 480 × 160 cells. Contour lines vary from 0.1 to 6.4 with an interval of 0.21.

4 Conclusion

In this study, we have proposed a new formulation for 3-point MCV scheme. Two fourth-order schemes, i.e. MCV3-4L and MCV3-4R, are derived by employing the additional DOFs defined at the center of left and right neighboring cells. A new BGS algorithm, underlying the ENO concept, has been proposed to design a non-oscillatory multi-moment scheme without degrading the fourth-order accuracy.

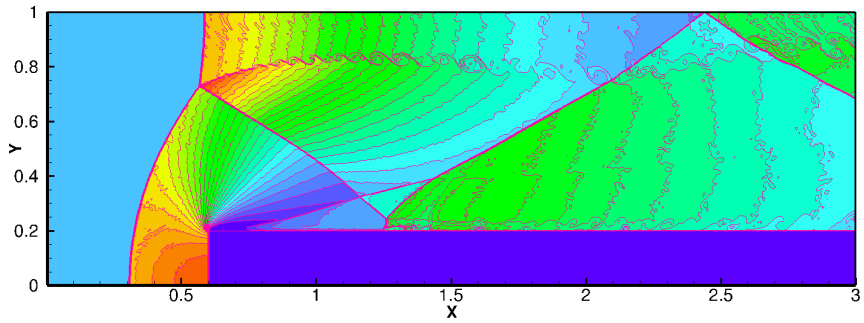

Fig. 17 Same as Fig.16, but with 960×320 cells.

The basic idea of the BGS algorithm is to choose a spatial reconstruction between MCV3-4L and MCV3-4R schemes, which minimizes the difference in the derivatives of flux functions between the high-order profile and the reconstruction with a slope limiter. This algorithm is easy to implement and free of and case-dependent ad hoc parameter. Thus, it is very proposing for practical applications.

Compared to other existing methods, the present scheme has at least following advantages.

1. Without any limiting process using either slope limiters or flux limiters, the proposed scheme doesn't suffer from loss of accuracy since a high-order reconstruction, either MCV3-4L or MCV3-4R is effectively adopted.
2. MCV3-BGS scheme does not need the priori detector, such as the TVB criterion, to peak up the "troubled cells". With effective oscillation-suppressing mechanism and well-controlled numerical dissipation, MCV3-BGS scheme resolves both smooth and discontinuous solutions.
3. Using the sub-grid DOFs, the spatial stencil used by MCV3-BGS is limited within three neighboring cells, which is very compact and suited for the grids with complex structures.

The performance of the proposed scheme is verified by the widely used benchmark tests for both scalar and Euler equations. The numerical results reveal that MCV3-BGS scheme is a high-fidelity scheme with local high order reconstruction that resolves both smooth and non-smooth solutions with appealing accuracy the robustness.

References

1. Chen, C.G., Xiao, F.: An adaptive multimoment global model on a cubed sphere. Mon. Wea. Rev. **139**, 523–548 (2011)
2. Cockburn, B., Lin, S.Y., Shu, C.W.: TVB Runge-Kutta local projection discontinuous Galerkin finite element method for conservation laws III: One-dimensional systems. J. Comput. Phys. **84**, 90–113 (1989)
3. Cockburn, B., Shu, C.W.: TVB Runge-Kutta local projection discontinuous Galerkin finite element method for conservation laws II: General framework. Math. Comput. **52**, 411–435 (1989)
4. Fan, P., Shen, Y., Tian, B., Yang, C.: A new smoothness indicator for improving the weighted essentially non-oscillatory scheme. J. Comput. Phys. **269**, 329–354 (2014)

5. Godlewski, E., Raviart, P.A.: Numerical approximation of hyperbolic systems of conservation laws, *Applied Mathematical Sciences*, vol. 118. Springer-Verlag New York (1996)
6. Harten, A., Engquist, B., Osher, S., Chakravarthy, S.R.: Uniformly high order accurate essentially non-oscillatory schemes III. J. Comput. Phys. **71**, 231–303 (1987)
7. Hesthaven, J.S., Warburton, T.: Nodal discontinuous Galerkin methods: Algorithms, analysis and applications. Springer-Verlag New York (2008)
8. Huang, C.S., Xiao, F., Arbogast, T.: Fifth order multi-moment weno schemes for hyperbolic conservation laws. J. Sci. Comput. **64**(2), 477–507 (2015)
9. Ii, S., Xiao, F.: CIP/multi-moment finite volume method for Euler equations, a semiLagrangian characteristic formulation. J. Comput. Phys. **222**, 849–871 (2007)
10. Ii, S., Xiao, F.: High order multi-moment constrained finite volume method. Part I: Basic formulation. J. Comput. Phys. **228**, 3669–3707 (2009)
11. Jiang, G.S., Shu, C.W.: Efficient implementation of weighted ENO Schemes. J. Comput. Phys. **126**, 202–228 (1996)
12. Li, X.L., Chen, C.G., Shen, X.S., Xiao, F.: A multi-moment constrained finite-volume model for nonhydrostatic atmospheric dynamics. Mon. Wea. Rev. **141**, 1216–1240 (2013)
13. Onodera, N., Aoki, T., Yokoi, K.: A fully conservative high-order upwind multi-moment method using moments in both upwind and downwind cells. Int. J. Numer. Meth. Fluids (2016). DOI 10.1002/fld.4228
14. Qiu, J.X., Shu, C.W.: Hermite WENO schemes and their application as limiters for Runge-Kutta discontinuous Galerkin method: one-dimensional case. J. Comput. Phys. **193**, 115–135 (2004)
15. Qiu, J.X., Shu, C.W.: Runge-Kutta discontinuous Galerkin method using WENO limiters. SIAM J. Sci. Comput. **26**, 907–929 (2005)
16. Shu, C.W., Osher, O.: Efficient implementation of essentially non-oscillatory shock capturing schemes II. J. Comput. Phys. **83**, 32–78 (1989)
17. Shu, C.W., Osher, S.: Efficient implementation of essentially non-oscillatory shockcapturing schemes. J. Comput. Phys. **77**, 439–471 (1988)
18. Sod, G.: A survey of several finite difference methods for systems of nonlinear hyperbolic conservation laws. J. Comput. Phys. **27**, 1–31 (1978)
19. Spiteri, R., Ruuth, S.J.: A new class of optimal high-order strong-stability-preserving time discretization methods. SIAM J. Numer. Anal. **40**, 469–491 (2002)
20. Sun, Y., Wang, Z.J., Liu, Y.: High-order multidomain spectral difference method for the Navier-Stokes equations on unstructured hexahedral grids. Comm. in Comput. Phys. **2**, 310–333 (2007)
21. Sun, Z.Y., Teng, H.H., Xiao, F.: A slope constrained 4th order multi-moment finite volume method with WENO limiter. Comm. in Comput. Phys. **18**, 901–930 (2015)
22. Toro, E.F.: Riemann solvers and numerical methods for fluid dynamics: a practical introduction, third edn. Springer-Verlag Berlin Heidelberg (2009)
23. Wang, Z.J.: Spectral (finite) volume method for conservation laws on unstructured grids: basic formulation. J. Comput. Phys. **178**, 210–251 (2002)
24. Woodward, P., Colella, P.: The numerical simulation of two-dimensional fluid flow with strong shocks. J. Comput. Phys. **54**, 115–173 (1984)
25. Xiao, F., T.Yabe: Completely conservative and oscillationless semi-lagrangian schemes for advection transportation. J. Comput. Phys. **170**, 498–522 (2001)
26. Xie, B., Ii, S., Ikebata, A., Xiao, F.: A multi-moment finite volume method for incompressible Navier-Stokes equations on unstructured grids: Volume-average/point-value formulation. J. Comput. Phys. **227**, 138–162 (2014)
27. Xie, B., Xiao, F.: Two and three dimensional multi-moment finite volume solver for incompressible Navier-Stokes equations on unstructured grids with arbitrary quadrilateral and hexahedral elements. Comput. Fluids **227**, 40–54 (2014)
28. Yabe, T., Aoki, T.: A universal solver for hyperbolic equations by cubic-polynomial interpolation I. One-dimensional solver. Comput. Phys. Commun. **66**, 219–232 (1991)
29. Yabe, T., Xiao, F., Utsumi, T.: The constrained interpolation profile method for multiphase analysis. J. Comput. Phys. **169**, 556–593. (2001)
30. Zhong, X., Shu, C.W.: A simple weighted essentially nonoscillatory limiter for Runge-Kutta discontinuous Galerkin methods. J. Comput. Phys. **232**, 397–415 (2013)